Available online at www.sciencedirect.com
ScienceDirect
International Journal of Multiphase Flow 32 (2006) 1055–1071
International Journal of Multiphase Flow
www.elsevier.com/locate/ijmulflow

Buoyancy-driven motion and breakup of viscous drops in constricted capillaries

Ufuk Olgac, Arif D. Kayaalp, Metin Muradoglu *

Department of Mechanical Engineering, Koc University, Rumelifeneri Yolu, Sariyer, 34450 Istanbul, Turkey

Received 12 July 2005; received in revised form 7 May 2006

Abstract

Buoyancy-driven motion and breakup of viscous drops in sinusoidally constricted channels are studied computationally using a finite-volume/front-tracking (FV/FT) method. Computational results are first compared with the available experimental data and then the conditions for a drop breakup are examined. The effects of the channel geometry, drop size and Bond number on drop breakup are investigated. It is found that the present computational results are in a good agreement with the available experimental data and drop breakup occurs in various modes depending on the channel geometry, the relative drop size and Bond number. It is observed that a drop breaks up into two or more drops when its size is larger than a critical value. It is also found that large drops undergo successive breakups to produce monodispersed small droplets. Critical non-dimensional drop size and critical capillary number for the onset of drop breakup are reported over a wide range of geometrical parameters and Bond numbers.

Keywords: Buoyancy-driven motion; Drop breakup; Constricted channel; Finite-volume/front-tracking method

1. Introduction

The motion and breakup of deformable drops and bubbles through constant and variable cross-section capillaries are of fundamental importance as a prototype problem in many engineering and scientific applications and natural processes. Examples include microfluidic systems (Stone et al., 2004), oil recovery by chemical flooding (Larson et al., 1981; Olbricht, 1996), and chemical and biological processes (Fauci and Gueron, 2001; Pozrikidis, 2003; Stone, 1994). Straight cylindrical capillaries were used extensively as a pore-scale model in early studies (Ho and Leal, 1975; Olbricht, 1996). However, in many engineering and scientific applications, the individual pores or channels are tortuous with rapid changes in the local cross-sectional area. To include this feature, constricted channels have been proposed as prototype pore-scale models (Gauglitz and Radke, 1990; Hemmat and Borhan, 1996; Olbricht and Leal, 1983; Olbricht, 1996). In particular, periodically constricted capillary has attracted considerable interest since they render the flow

* Corresponding author. Tel.: +90 212 338 14 73; fax: +90 212 338 15 48.
E-mail address: mmuradoglu@ku.edu.tr (M. Muradoglu).

0301-9322/$ - see front matter © 2006 Elsevier Ltd. All rights reserved.
doi:10.1016/j.ijmultiphaseflow.2006.05.004

unsteady in a Lagrangian sense with the reproduction of certain features of the flow kinematics, which can have significant influence on the mobility of the drop and drop breakup (Hemmat and Borhan, 1996; Olbricht and Leal, 1983; Olbricht, 1996).

In the context of the present work, the most relevant experimental studies on the motion of drops in capillaries have been performed by Olbricht and Leal (1983) and Hemmat and Borhan (1996). Olbricht and Leal (1983) considered the motion of immiscible neutrally buoyant drops in pressure-driven flow through a horizontal capillary whose diameter varies periodically with axial position. They measured the average drop speed and correlated those values with the observed time-dependent drop shapes. Their results were mainly qualitative and demonstrated the effect of capillary geometry on the shape and mobility of drops. Hemmat and Borhan (1996) reported the buoyancy-driven motion of viscous drops and gas bubbles through a vertical capillary with periodic constrictions in order to examine the effects of capillary geometry on drop deformation and breakup. Some of the experimental cases studied by Hemmat and Borhan (1996) are used in the present work to validate the computational results.

On the theoretical and computational side, the previous studies have been mostly restricted to the straight cylindrical or polygonal capillaries with uniform cross-sectional areas as reviewed by Olbricht (1996). However, a number of theoretical and computational investigations of the motion and breakup of drops and bubbles in variable cross-section channels have been also reported, for example, by Westborg and Hassager (1989), Gauglitz and Radke (1990) and Tsai and Miksis (1994, 1997) but almost all in the limiting case of creeping flow regime. In constricted channels, flow is inherently unsteady and inertial effects might be important. Especially in the case of small capillary numbers or severely constricted channels, the finite Reynolds number effects must be taken into account (Olbricht, 1996). Recently Muradoglu and Gokaltun (2004) have studied the motion of two-dimensional buoyancy-driven drops through sinusoidally constricted channels with finite Reynolds numbers but have not reported any drop breakup in the cases they studied. Drop breakup is of fundamental importance as it is the key process that determines the critical conditions for the existence of steady drop shapes and the final drop distribution in a multiphase system (Stone, 1994).

In the present paper, we consider the motion and breakup of axisymmetrical buoyancy-driven viscous drops through sinusoidally constricted capillaries. Computations are performed using a finite-volume/front-tracking method developed by Muradoglu and Kayaalp (2006). The governing equations for axisymmetric geometry are solved numerically on a curvilinear grid using a finite-volume method. The drop interface is represented by connected Lagrangian marker points which move with the local flow velocity. The flow equations are written for the entire computational domain and different phases are treated as a single fluid with variable material properties. The effect of the surface tension is taken into account by treating them as body forces in the same way as described by Unverdi and Tryggvason (1992). The method is first applied to the cases studied experimentally by Hemmat and Borhan (1996) and the results are compared with the experimental data. It is found that the present computational results are in a good agreement with the available experimental data. Then the method is used to study the effects of the drop size, the channel geometry and Bond number on the motion and breakup of viscous drops in constricted capillaries. It is shown that a viscous drop breaks up into smaller drops when the non-dimensional drop size exceeds a critical value as was experimentally observed by Hemmat and Borhan (1996). The breakup is usually initiated with the retarding effect of the constrictions. It is found that different modes of breakup occur at various Bond numbers and channel geometries. Although it is widely believed that tail streaming occurs due to accumulation of surfactant (Borhan and Pallinti, 1995, 1999), a breakup mode is observed that resembles the tail streaming.

In the next section, the governing equations and the numerical solution algorithm are briefly reviewed. The physical problem is described in Section 3 where the results and discussions are also presented. Finally, some conclusions are drawn in Section 4.

2. Mathematical formulation and numerical algorithm

The governing equations are described in this section in the context of the finite-volume/front-tracking method. Following Unverdi and Tryggvason (1992) and Muradoglu and Kayaalp (2006), the incompressible flow equations for an axisymmetric flow can be written in the cylindrical coordinates in the vector form as

$$\frac{\partial \mathbf{q}}{\partial t}+\frac{\partial \mathbf{f}}{\partial r}+\frac{\partial \mathbf{g}}{\partial z}=\frac{\partial \mathbf{f}_{\mathrm{v}}}{\partial r}+\frac{\partial \mathbf{g}_{\mathrm{v}}}{\partial z}+\mathbf{h}_{\mathrm{v}}+\mathbf{f}_{\mathrm{b}}, \tag{1}$$

where

$$\mathbf{q}=\begin{Bmatrix} 0 \\ r\rho v_r \\ r\rho v_z \end{Bmatrix}, \qquad \mathbf{f}=\begin{Bmatrix} rv_r \\ r(\rho v_r^2+p) \\ r\rho v_r v_z \end{Bmatrix}, \qquad \mathbf{g}=\begin{Bmatrix} rv_z \\ r\rho v_r v_z \\ r(\rho v_z^2+p) \end{Bmatrix} \tag{2}$$

and

$$\mathbf{f}_{\mathrm{v}}=\begin{Bmatrix} 0 \\ \tau_{rr} \\ \tau_{zr} \end{Bmatrix}, \qquad \mathbf{g}_{\mathrm{v}}=\begin{Bmatrix} 0 \\ \tau_{zr} \\ \tau_{zz} \end{Bmatrix}, \qquad \mathbf{h}_{\mathrm{v}}=\begin{Bmatrix} 0 \\ p-\frac{2}{r}\frac{\partial}{\partial r}(r\mu v_r)-\frac{\partial}{\partial z}(\mu v_z) \\ -\frac{\partial}{\partial z}(\mu v_z) \end{Bmatrix}. \tag{3}$$

In Eqs. (1)–(3), r and z are the radial and axial coordinates and t is the physical time; ρ, μ and p are the fluid density, the dynamic viscosity and pressure; v_r and v_z are the velocity components in r and z coordinate directions, respectively. The viscous stresses appearing in the viscous flux vectors are given by

$$\tau_{rr}=2\mu\frac{\partial rv_r}{\partial r}, \qquad \tau_{zz}=2\mu\frac{\partial rv_z}{\partial z}, \qquad \tau_{zr}=\mu\left(\frac{\partial rv_r}{\partial z}+\frac{\partial rv_z}{\partial r}\right). \tag{4}$$

The last term in Eq. (1) represents the body forces resulting from the buoyancy and surface tension and is given by

$$\mathbf{f}_{\mathrm{b}}=-r(\rho_{\mathrm{o}}-\rho)\mathbf{g}_z-\int_S r\sigma\kappa\mathbf{n}\delta(\mathbf{x}-\mathbf{x}_f)\,\mathrm{d}s, \tag{5}$$

where the first term represents the body force due to buoyancy with ρ_{o} and $\mathbf{g}_z$ being the density of ambient fluid and the gravitational acceleration, respectively. The second term in Eq. (5) represents the body force due to the surface tension, and δ, $\mathbf{x}_{\mathrm{f}}$, σ, κ, $\mathbf{n}$, S and $\mathrm{d}s$ denote the Dirac delta function, the location of the front, the surface tension coefficient, twice the mean curvature, the outward unit normal vector on the interface, the surface area of the interface and the surface area element of the interface, respectively.

In Eq. (1), the fluids are assumed to be incompressible and the effects of heat transfer are neglected. Therefore, the density and the viscosity of a fluid particle remain constant, i.e., $\frac{\mathrm{D}\rho}{\mathrm{D}t}=0$ and $\frac{\mathrm{D}\mu}{\mathrm{D}t}=0$, where the substantial derivative is defined as $\frac{\mathrm{D}}{\mathrm{D}t}=\frac{\partial}{\partial t}+\mathbf{u}\cdot\nabla$.

As can be seen in Eq. (1), the continuity equation is decoupled from the momentum equations since it does not have any time derivative term. In order to overcome this difficulty and to be able to use a time-marching solution algorithm, artificial time derivative terms are added to the flow equations in the form

$$\Gamma^{-1}\frac{\partial \mathbf{w}}{\partial \tau}+\mathbf{I}^1\frac{\partial \rho\mathbf{w}}{\partial t}+\frac{\partial \mathbf{f}}{\partial r}+\frac{\partial \mathbf{g}}{\partial z}=\frac{\partial \mathbf{f}_{\mathrm{v}}}{\partial r}+\frac{\partial \mathbf{g}_{\mathrm{v}}}{\partial z}+\mathbf{h}_{\mathrm{v}}+\mathbf{f}_{\mathrm{b}}, \tag{6}$$

where τ is the pseudo time. The solution vector $\mathbf{w}$, the incomplete identity matrix I^1 and the preconditioning matrix Γ^{-1} are given by

$$\mathbf{w}=\begin{Bmatrix} rp \\ rv_r \\ rv_z \end{Bmatrix}, \qquad I^1=\begin{bmatrix} 0 & 0 & 0 \\ 0 & 1 & 0 \\ 0 & 0 & 1 \end{bmatrix}, \qquad \Gamma^{-1}=\begin{bmatrix} \frac{1}{\rho\beta^2} & 0 & 0 \\ 0 & \rho & 0 \\ 0 & 0 & \rho \end{bmatrix}, \tag{7}$$

where β is the preconditioning parameter with dimensions of velocity (Muradoglu and Kayaalp, 2006). A detailed description of the pseudo time-stepping method can be found in Caughey (2001) and Muradoglu and Kayaalp (2006).

With the goal of treating complex geometries, Eq. (6) can be transformed into a general, curvilinear coordinate system

$$\xi=\xi(r,z), \qquad \eta=\eta(r,z) \tag{8}$$

and the resulting equations take the form

$$\Gamma^{-1}\frac{\partial h\mathbf{w}}{\partial \tau}+\mathbf{I}^{1}\frac{\partial \rho h\mathbf{w}}{\partial t}+\frac{\partial h\mathbf{F}}{\partial \xi}+\frac{\partial h\mathbf{G}}{\partial \eta}=\frac{\partial h\mathbf{F}_{\mathrm{v}}}{\partial \xi}+\frac{\partial h\mathbf{G}_{\mathrm{v}}}{\partial \eta}+h(\mathbf{h}_{\mathrm{v}}+\mathbf{f}_{\mathrm{b}}), \tag{9}$$

where $h=r_{\xi}z_{\eta}-r_{\eta}z_{\xi}$ represents the Jacobian of the transformation. The vectors $h\mathbf{F}=z_{\eta}\mathbf{f}-r_{\eta}\mathbf{g}$; $h\mathbf{G}=-z_{\xi}\mathbf{f}+r_{\xi}\mathbf{g}$ and $h\mathbf{F}_{\mathrm{v}}=z_{\eta}\mathbf{f}_{\mathrm{v}}-r_{\eta}\mathbf{g}_{\mathrm{v}}$; $h\mathbf{G}_{\mathrm{v}}=-z_{\xi}\mathbf{f}_{\mathrm{v}}+r_{\xi}\mathbf{g}_{\mathrm{v}}$, represent the transformed inviscid and viscous flux vectors, respectively.

The governing equations (Eq. (9)) are solved using the finite-volume/front-tracking method developed by Muradoglu and Kayaalp (2006). The method combines a finite-volume solver with the front-tracking method developed by Unverdi and Tryggvason (1992). In this method, the spatial derivatives are discretized using a finite-volume method that is equivalent to a second order finite-differences on a uniform Cartesian mesh. Time integration in pseudo time is achieved by an alternating direction implicit (ADI) method (Beam and Warming, 1978). Fourth-order numerical dissipation terms are added to the discrete version of the flow equations in the form described by Caughey (1988) to prevent the odd–even decoupling. Several convergence acceleration techniques including the local time-stepping, preconditioning and multigrid methods are used to accelerate the convergence rate of the ADI method in pseudo time. A three point second order backward implicit method is used to approximate the physical time derivatives.

Three types of grids used in the present method are sketched in Fig. 1. Conservation equations are solved on a body-fitted curvilinear grid and the interface is represented by connected Lagrangian marker points moving with the local flow velocity interpolated from the neighboring grid points. A piece of the interface between two neighboring marker points is called a front element. The communication between the curvilinear grid and the interface marker points is maintained efficiently using an auxiliary Cartesian grid cast on the curvilinear grid as shown in Fig. 1. The material properties inside and outside the drop are set based on the indicator function defined such that it is unity inside the droplet and zero outside. The indicator function is computed on the regular Cartesian grid using the procedure described by Tryggvason et al. (2001) and then it is interpolated on the curvilinear grid using bilinear interpolations. The interface marker points are also used to compute the surface tension forces at the interface which are then distributed on the neighboring curvilinear grid cells as a body forces in a conservative manner. The details of the FV/FT method can be found in Muradoglu and Gokaltun (2004) and Muradoglu and Kayaalp (2006).

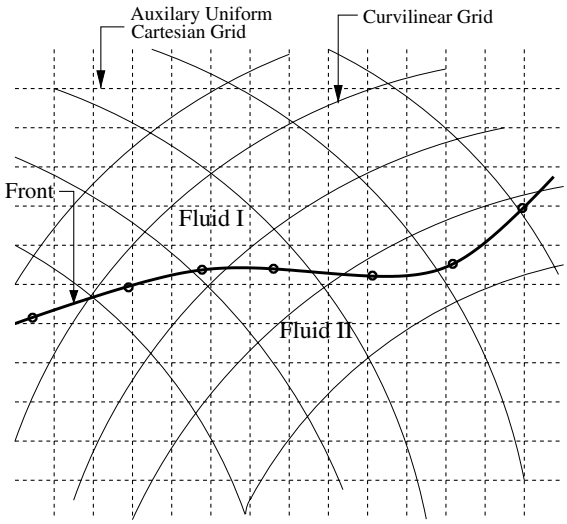

Fig. 1. Three types of grids used in the computations. The governing equations are solved on a fixed Eulerian curvilinear grid and the interface between different phases is represented by a Lagrangian grid consisting of connected marker points. An auxiliary uniform Cartesian grid is used to maintain communication between the curvilinear and Lagrangian grids (Muradoglu and Kayaalp, 2006).

3. Results and discussion

The finite-volume/front-tracking method is first applied to the cases studied experimentally by Hemmat and Borhan (1996) and then it is used to determine the conditions for the breakup of viscous drops in constricted capillaries.

The physical problem and the computational domain are sketched in Fig. 2a and a portion of a coarse curvilinear grid containing 8×416 grid cells is plotted in Fig. 2b to show the overall structure of the computational grid. Note that most of the computations are performed using finer versions of this grid, i.e., typically containing 32×1664 grid cells. In Fig. 2a, the left boundary is the axis of symmetry and all other boundaries are solid walls where no-slip boundary conditions are applied. The geometric parameters R, R_{th}, A, h and H represent the average capillary radius, the minimum capillary radius at throat, the corrugation amplitude, the corrugation wavelength and the channel height, respectively. A drop with diameter d and radius R_d is instantaneously placed in the ambient fluid that fully fills the cylindrical tube. The drop is initially spherical if its initial radius is smaller than the radius of the capillary tube and is ellipsoidal otherwise. Note that d represents the equivalent drop diameter if the initial shape of the drop is not spherical. The drop has a viscosity μ_d and a density ρ_d while the ambient fluid has a viscosity μ_o and a density ρ_o. The drop starts rising due to buoyancy forces caused by the density difference $\Delta\rho = \rho_o - \rho_d$ and a constant gravitational acceleration denoted by g. The viscosity and density ratios are defined as $\lambda = \mu_d/\mu_o$ and $\gamma = \rho_d/\rho_o$, respectively. The geometry of the channel is characterized by two non-dimensional parameters, namely, the ratio of the amplitude of corrugation to the average channel radius $\alpha = A/R$ and the ratio of the corrugation wavelength to the average channel radius $\eta = h/R$. The first parameter (α) characterizes the channel constriction level and is referred hereafter as the channel constriction parameter or simply constriction parameter while the second parameter (η) is the non-dimensional corrugation wavelength. The ratio of the channel at throat to the equivalent drop radius $\Lambda = R_{th}/R_d$ is also an important parameter that critically influences deformation

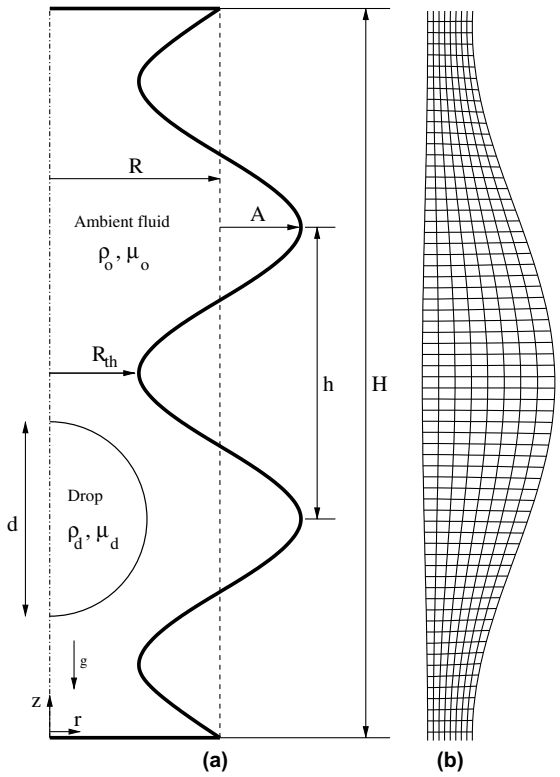

Fig. 2. (a) Schematic illustration of the computational setup for a buoyancy-driven rising drop in a constricted channel for $\alpha = 0.50$. (b) A portion of a coarse computational grid containing 8×416 cells.

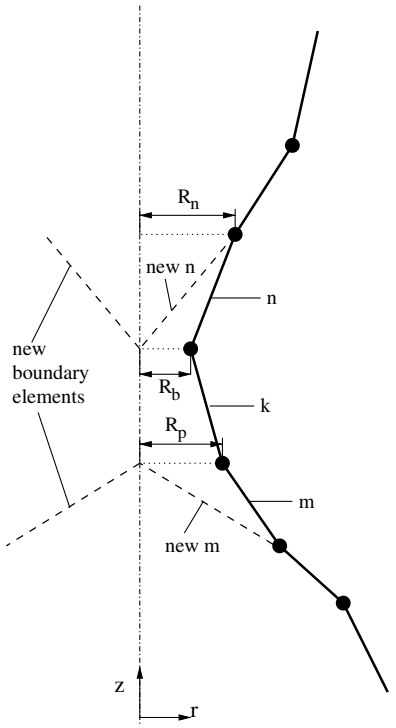

Fig. 3. Treatment of a drop breakup. The front element k is deleted when R_b is smaller than a prespecified threshold value R_{break}, the marker points are projected on the centerline and new boundary elements are created as shown.

and breakup of the drop. The non-dimensional drop radius is defined as the ratio of the equivalent spherical drop radius to the average capillary radius $\kappa = R_d/R$. The Bond number is defined as $Bo = \Delta\rho g\ R^2/\sigma$ representing the ratio of buoyancy forces to the interfacial forces.

The results are expressed in terms of non-dimensional quantities denoted by superscript "$*$". The dimensionless coordinates are defined as $z^* = z/h$ and $r^* = r/R$. Time and velocity are made dimensionless with the reference values of $T_{ref} = \frac{\mu_o}{\Delta\rho g R}$ and $V_{ref} = \frac{\Delta\rho g R^2}{\mu_o}$, respectively.

It is assumed that a drop breakup occurs when the radius at the neck is smaller than a prespecified threshold value, R_{break}. For this purpose, the radius at the neck is monitored during the computation and when the neck radius is smaller than R_{break}, the front element that is closest to the centerline at the neck is deleted. After that the marker points at both ends of the deleted element are projected on the centerline and new boundary elements are created as shown in the sketch in Fig. 3. The threshold value is taken as the smallest curvilinear grid size in the present computations and it is found that the results are not sensitive to the choice of the threshold value as long as it is of order of the local grid size. This simple treatment of breakup is found to be very robust and gives reasonably good results compared to the experimental data as discussed in the following section.

3.1. Comparison with experimental data

In the experimental setup (Hemmat, 1996; Hemmat and Borhan, 1996), the capillary tube consists of a 26 cm long, periodically constricted cylindrical tube with six corrugations. The internal radius of the capillary tube is $R = 0.5$ cm, the wavelength of the corrugations is $h = 4$ cm and the amplitude of the corrugations is $A = 0.07$ cm corresponding to the geometric parameters $\alpha = 0.14$ and $\eta = 8$. The suspending fluids are aqueous glycerol solutions (denoted by GW3 and GW5) and diethylene glycol–glycerol mixtures (denoted by DEGG10 and DEGG12). A variety of UCON oils are used as drop fluids. The properties of the drop and suspending fluids are summarized in Table 1 where the same label is used for each system as used by Hemmat and Borhan (1996). A complete description of the experimental set up can be found in Hemmat (1996) and Hemmat and Borhan (1996). We consider four systems labeled as GW3, GW5, DEGG10 and DEGG12 (Table 1). It is

emphasized here that, in addition to the reported measurement error up to 5% in the experimental data, there is inconsistency between the material properties and the non-dimensional numbers especially for DEGG12 system. For instance, the Bond number reported by Hemmat and Borhan (1996) is about 10% larger than the value we computed directly from the given material properties and the average tube radius.

First a qualitative analysis for the evolution of the drop shapes is presented. For this purpose, sequences of images illustrating the evolution of the shapes of viscous drops as they move through the constricted channel are plotted in Fig. 4 for GW3, DEGG12 and GW5 systems with the non-dimensional drop sizes of $\kappa = 0.54$, 0.78 and 0.92. The computations are performed using a 32×1664 grid, the physical time step is $\Delta t^* = 1.641$

Table 1
Two-phase systems used both in the experiments (Hemmat, 1996; Hemmat and Borhan, 1996) and in the present computations

System	Suspending fluid	Drop fluid	μ_o (mPa s)	μ_d (mPa s)	ρ_o (kg/m^3)	ρ_d (kg/m^3)	σ (N/m)
GW3	Glycerol–water (96.2 wt%)	UCON-1145	450	530	1250	995	0.0105
GW5	Glycerol–water (96.2 wt%)	UCON-50HB100	450	97	1250	950	0.0057
DEGG10	Diethylene–glycol (100.0 wt%)	UCON-165	28	63	1110	975	0.0016
DEGG12	Diethylene glycol–glycerol (63.8 wt%)	UCON-285	87	115	1160	966	0.0042

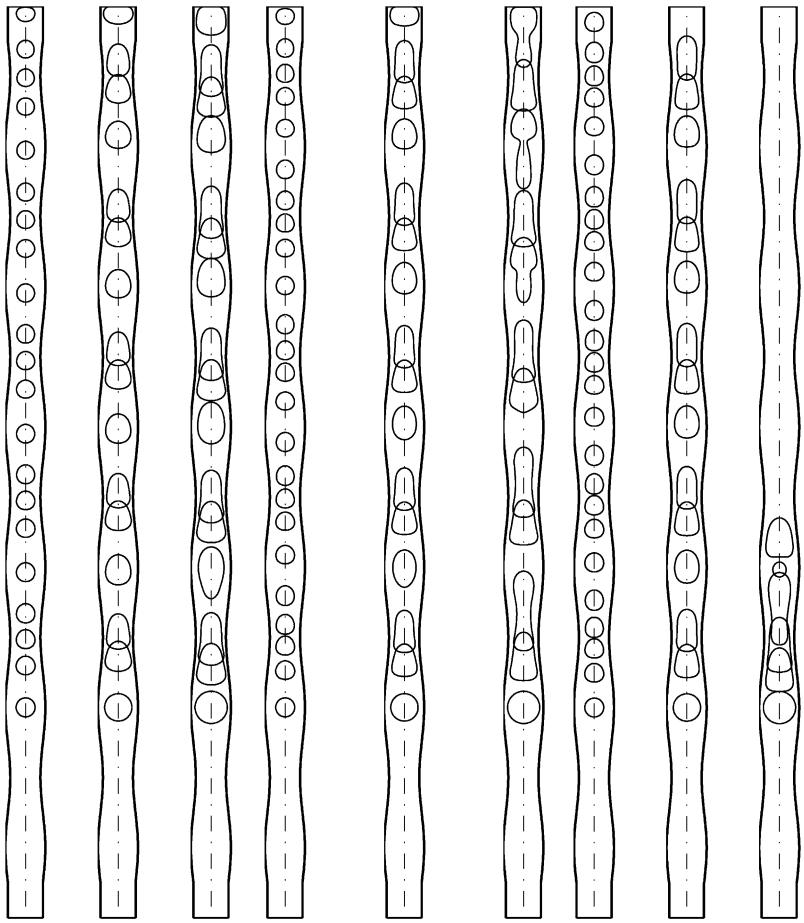

Fig. 4. Snapshots of buoyant drops of (a) GW3 system, (b) DEGG12 system and (c) GW5 system for drops sizes $\kappa = 0.54$, 0.78 and 0.92 from left to right for each system. The gap between two successive drops in each column represents the distance the drop travels at a fixed time interval and the last interface is plotted from left to right at t^*: (a) 1044.4, 783.3, 783.3; (b) 2831.3, 3693.0, 5416.4; (c) 1883.5, 1785.4 and 486.6, respectively.

and the residuals are reduced by three orders of magnitude in each sub-iteration. It is emphasized that, although not shown here due to space considerations, these numerical parameters result in less than a few percent of total numerical discretization error for all the quantities in the case of DEGG12 system shown in Fig. 4b and it is expected that the numerical error is about the same order for other cases. The readers are referred to Muradoglu and Kayaalp (2006) for a detailed numerical error convergence analysis of the present finite-volume/front-tracking method. As can be seen in these figures, when a large drop ($\kappa > 0.7$) reaches a constriction, its leading edge follows the capillary wall contour and squeezes through the throat. Once the leading meniscus clears the throat, its rise velocity increases as it enters the diverging cross-section while the trailing edge of the drop remains trapped behind the throat. This behavior is in a very good agreement with the experimental observations (Hemmat and Borhan, 1996). As the non-dimensional drop size gets larger, this necking may lead to a breakup of the drop as seen in Fig. 4c. The non-dimensional drop size for which the drop starts to break up is called the critical drop size and is denoted by κ_{cr}. For GW5 system, it is found computationally that the critical drop radius is about $\kappa_{cr} = 0.87$ which is very close to the experimental value of $\kappa_{cr} = 0.85$ (Hemmat, 1996; Hemmat and Borhan, 1996). To better show the effects of the constrictions, the snapshots of the drops before and after the throat of the constriction are shown in Fig. 5 for GW3 system for drop sizes $\kappa = 0.54, 0.65, 0.78, 0.85$ and 0.92. No breakup is observed for GW3 system in this drop size range. As can be seen in this figure, the computed drop shapes com-

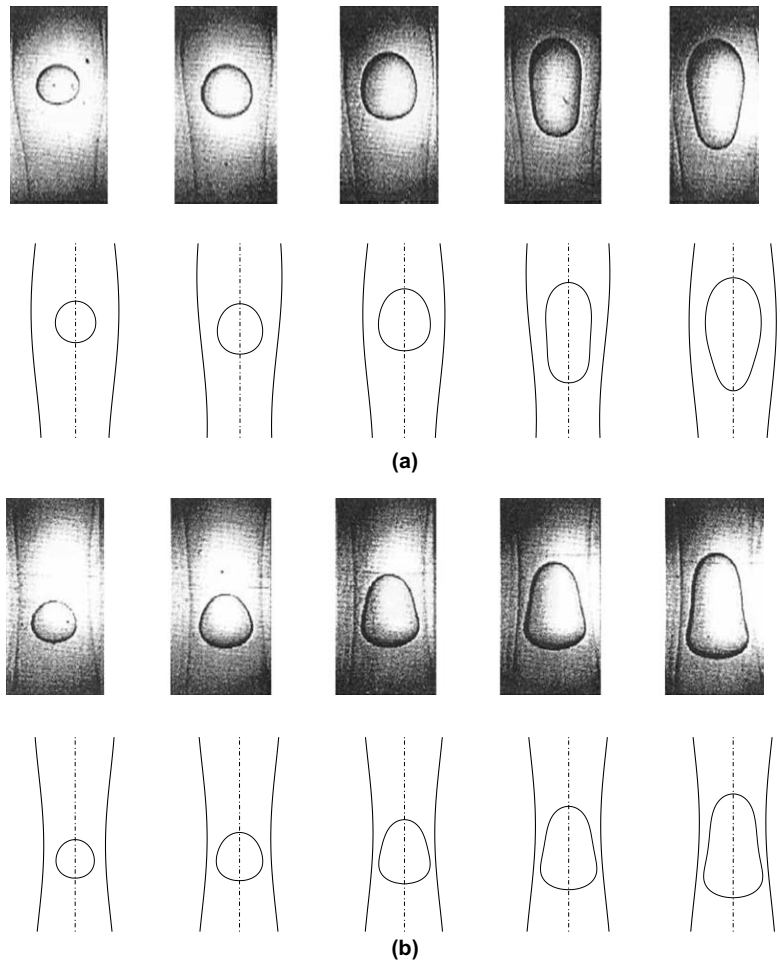

Fig. 5. Snapshots of the experimental (upper plots) and computed (lower plots) drop shapes at the expansion (a) and at the throat (b) of the constriction for the GW3 system for drop sizes (from left to right) $\kappa = 0.54, 0.65, 0.78, 0.85$ and 0.92, respectively. Grid: 32×1664, $\Delta t^* = 0.418$. Copyright (1996) From Buoyancy-driven Motion of Drops and Bubbles in a Periodically Constricted Capillary by Hemmat and Borhan. Reproduced by Permission of Taylor & Francis, Inc., http://www.taylorandfrancis.com.

pare well with the experimental pictures indicating the accuracy of the present simulations. A typical drop breakup is shown in Fig. 6. In this figure, the breakup process for a GW5 drop with the non-dimensional drop size of $\kappa = 0.90$ is illustrated through a series of snapshots taken just before and after the breakup. It is clearly seen in this figure that the computed drop shapes qualitatively compare well with the experimental observations showing the validity of the simple treatment of drop breakup used in the present study.

In order to quantify the motion and evolution of drops as they pass through the corrugations, a deformation parameter denoted by D is defined as the ratio of the perimeter of the deformed drop profile to that of the equivalent spherical drop. In addition, the non-dimensional axial length of the drop is defined as the axial length of drop profile scaled by the wavelength of corrugation and is denoted by L. Both D and L are plotted in Fig. 7 together with the experimental data within one period of corrugation for various values of drops sizes of GW3 system. As can be seen in this figure, the general trends both for D and L are well captured by the present computations. The deformation is negligibly small for small drops, i.e., drops with $\kappa < 0.60$, and increases rapidly as the drop size gets larger. The discrepancy between the computed and the experimental results for D and L are partly attributed to the uncertainties in the experimental data and to the inconsistency between the Bond number reported by Hemmat and Borhan (1996) and the Bond number computed from the material properties and the average tube radius as mentioned before.

Finally the computed average rise velocities are compared with the experimental data. The non-dimensional average rise velocity U_m is plotted against the non-dimensional drop size κ in Fig. 8a for GW3, GW5,

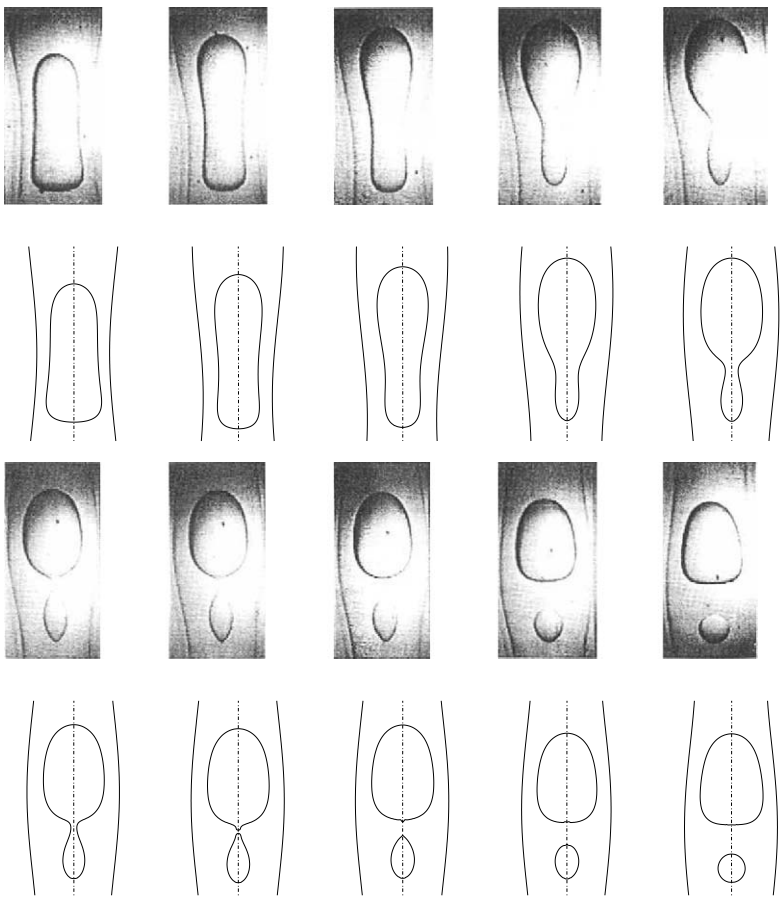

Fig. 6. Evolution of a GW5 drop with $\kappa = 0.90$ in the constricted channel. The drop size is greater than the critical value so the drop breaks up. The computed drop shapes (second and fourth rows) are plotted just below the experimental pictures (first and third rows) at approximately the same time frames ($\alpha = 0.14$ and $\kappa_{cr} = 0.87$). Copyright (1996) From Buoyancy-driven Motion of Drops and Bubbles in a Periodically Constricted Capillary by Hemmat and Borhan. Reproduced by Permission of Taylor & Francis, Inc., http://www.taylorandfrancis.com.

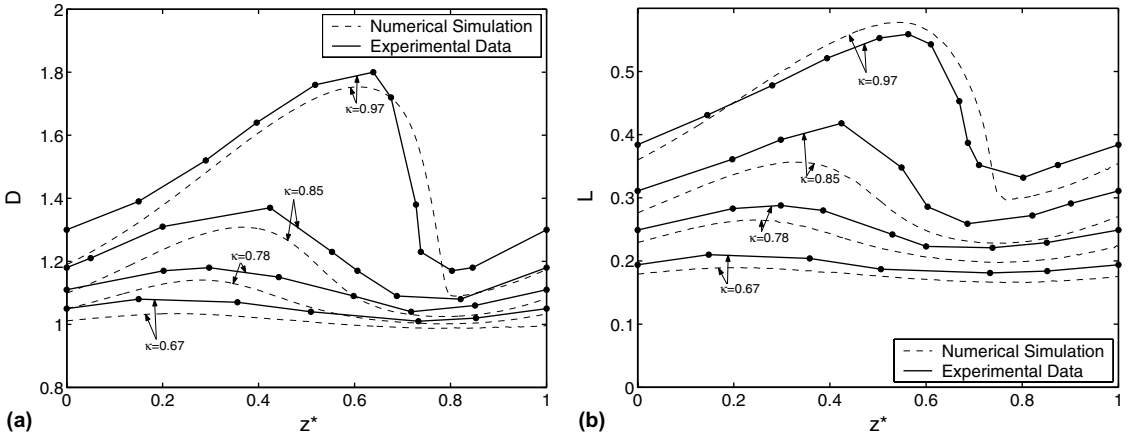

Fig. 7. The variations of (a) the deformation parameter D and (b) the nondimensional axial drop length L with nondimensional axial position of the advancing meniscus within one period of corrugation for GW3 system. The dashed curves are the numerical results and the solid lines are the experimental data.

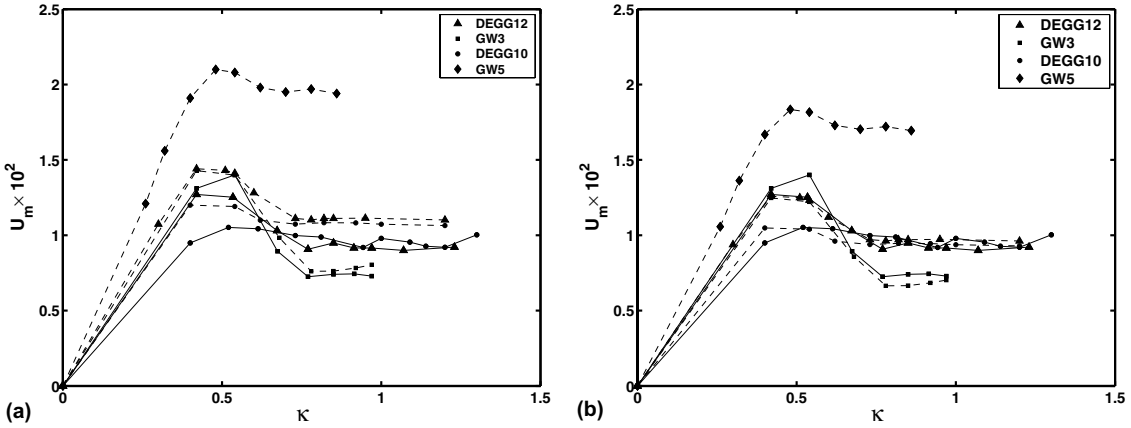

Fig. 8. Dimensionless average rise velocity as a function of the nondimensional drop radius. The dashed curves are the numerical results and the solid lines are the experimental data. The numerical results are obtained with (a) the average tube radius of $R = 0.5$ cm and (b) the modified tube radius of $R = 0.535$ cm that yields the same Bond number given by Hemmat and Borhan (1996).

DEGG10 and DEGG12 systems. The average rise velocity is defined as the average velocity of the drop centroid in the periodic motion. As can be seen in this figure, the numerical results are in a good agreement with the experimental data, i.e., the trend is well captured and the maximum error is less than 10% for all the cases. Note that there is no experimental data available for GW5 system but the numerical results for this system indicate a similar trend as the others. In addition, if the inconsistency between the Bond numbers mentioned above is taken into account by modifying the average tube radius to match the Bond number reported in Hemmat and Borhan (1996), the computed results compare much better with the experimental data as shown in Fig. 8b. In this case, the differences between the computed and experimental data reduce below a few percent at all the data points. In Fig. 8, the retardation effect of the constrictions is clearly seen and the non-dimensional velocity remains essentially constant for large drops, i.e., $\kappa > 0.90$ for all the cases.

3.2. Drop breakup

After validating the computational results against the experimental data in the previous section, we now investigate the conditions for the onset of breakup. In all the results presented in this section, GW5 system

is used as a base case. Note that $Bo = 12.91$ and $\alpha = 0.14$ correspond to the experimental conditions. The snapshots are shown in Fig. 9 for different values of the non-dimensional drop size and Bond number in the capillary tube with the constriction parameter $\alpha = 0.28$. In the absence of a drop breakup, the snapshots are taken at the positions where the maximum necking is expected to occur. As can be seen in this figure, the critical drop size gets smaller as the Bond number increases. At low Bond numbers, i.e., $Bo < 15$, a drop breaks up into two or more drops of comparable size. As the Bond number increases, a drop breaks up into a large leading drop and many small trailing drops until the size of the leading drop gets smaller than the critical drop size when the initial drop size is equal or slightly larger than the critical value. This breakup mode resembles the tail streaming that typically occurs due to accumulation of surfactant at the back of the drop (Borhan and Pallinti, 1995, 1999). On the other hand, if both the Bond number and drop size are large, the drops break up into two or more drops with comparable sizes, i.e., large drops undergo successive breakups to produce monodispersed small droplets. This can be visually seen in Fig. 9 and is verified in Fig. 10 where the volume of the

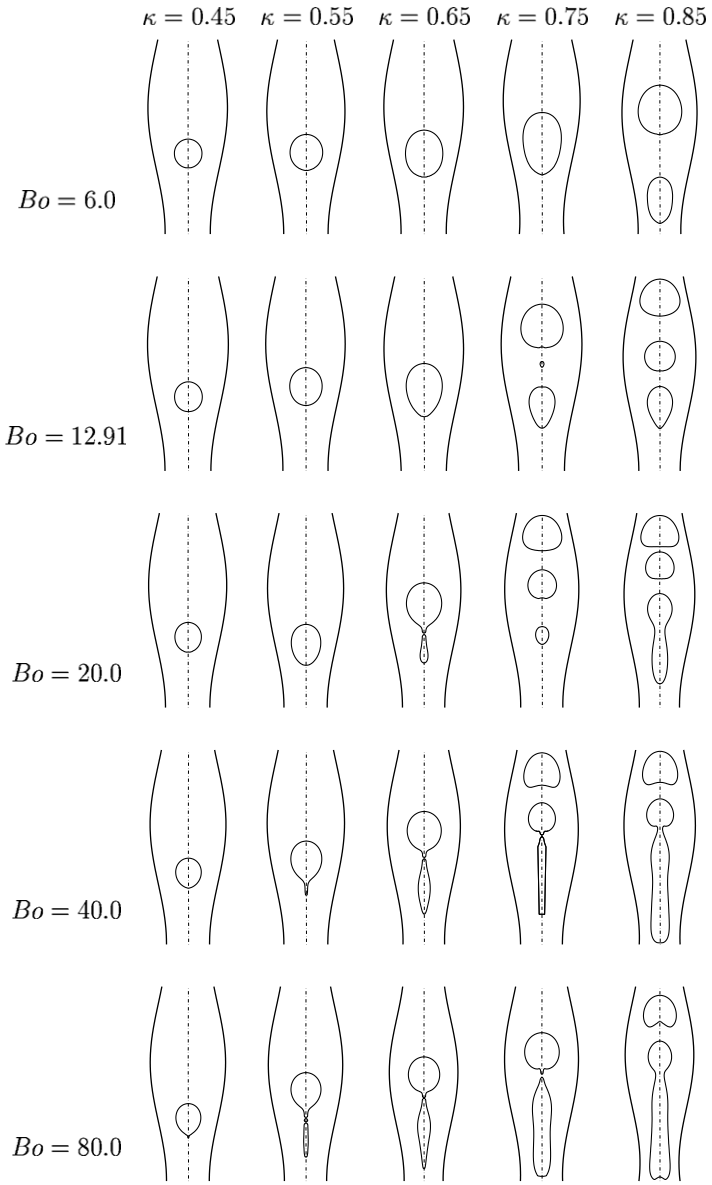

Fig. 9. The effects of the drop size and Bond number on drop breakup. (The plots are not in the same scale and $\alpha = 0.28$.)

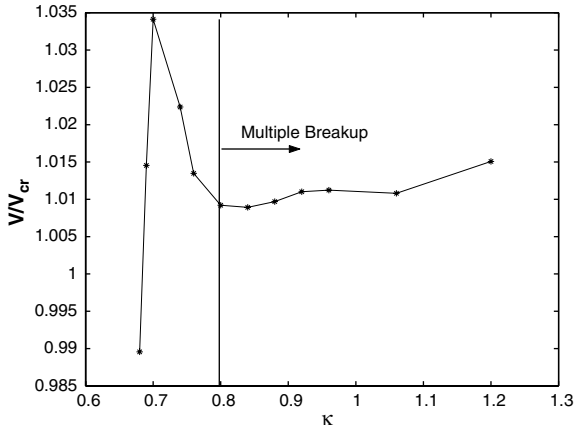

Fig. 10. Nondimensional leading drop volume for GW5 system as a function of the nondimensional drop size ranging between $\kappa = \kappa_{cr} = 0.68$ and $\kappa = 1.20$. The drop volume is normalized by the value obtained at the critical drop size ($\alpha = 0.28$, $Bo = 12.91$).

leading drop is plotted as a function of non-dimensional drop size. Note that the leading drop volume plotted in Fig. 10 is scaled by $V_{cr} = \frac{4}{3}\pi R_{cr}^3$ where R_{cr} is the critical drop radius for breakup. It is clearly seen in Fig. 10 that the leading drop volume remains nearly constant and multiple breakups occur when $\kappa > 0.8$ for this particular case. It is also seen in Fig. 9 that the trailing drop is small at critical drop size and increases rapidly as the size of the parent drop increases. To verify this observation, the ratio of the trailing drop volume to the leading drop volume is plotted in Fig. 11 as a function of non-dimensional drop size. As can be seen in this figure, trailing drop size is very small at the critical drop size and increases as the size of the parent drop increases. Note that, in the cases of multiple breakup, values are taken after the first breakup. Next the effects of the channel constriction on the evolution and breakup of the drops are shown in Fig. 12 for various Bond numbers. As can be seen in this figure, the critical drop size decreases as the level of constriction increases. At low Bond numbers, the drops may get stuck at the constrictions as seen in the case of $Bo = 6$ and $\alpha = 0.50$ in the figure. In this case, the buoyancy forces are not sufficient to force the drop through the constriction and are balanced by the surface tension forces leading eventually to a hydrostatic equilibrium. When the Bond number is made sufficiently large and the drop size is larger than the critical value, the drop breaks up into smaller drops in various modes as shown in the figure. Two representative examples are shown in Fig. 13 to better

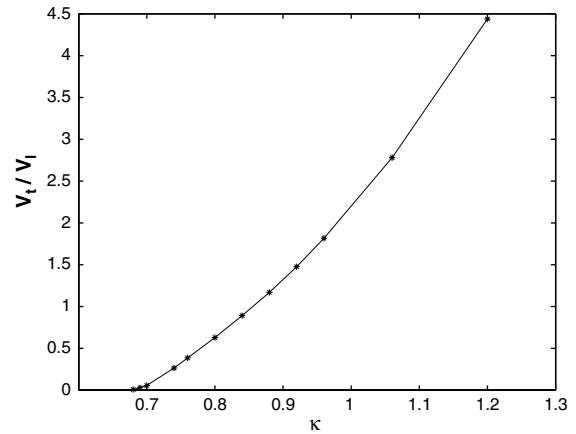

Fig. 11. Ratio of the trailing drop volume to the leading drop volume for GW5 system as a function of the nondimensional drop size ranging between $\kappa = \kappa_{cr} = 0.68$ and $\kappa = 1.20$. The values are taken after the first breakup in multiple breakup cases ($\alpha = 0.28$, $Bo = 12.91$).

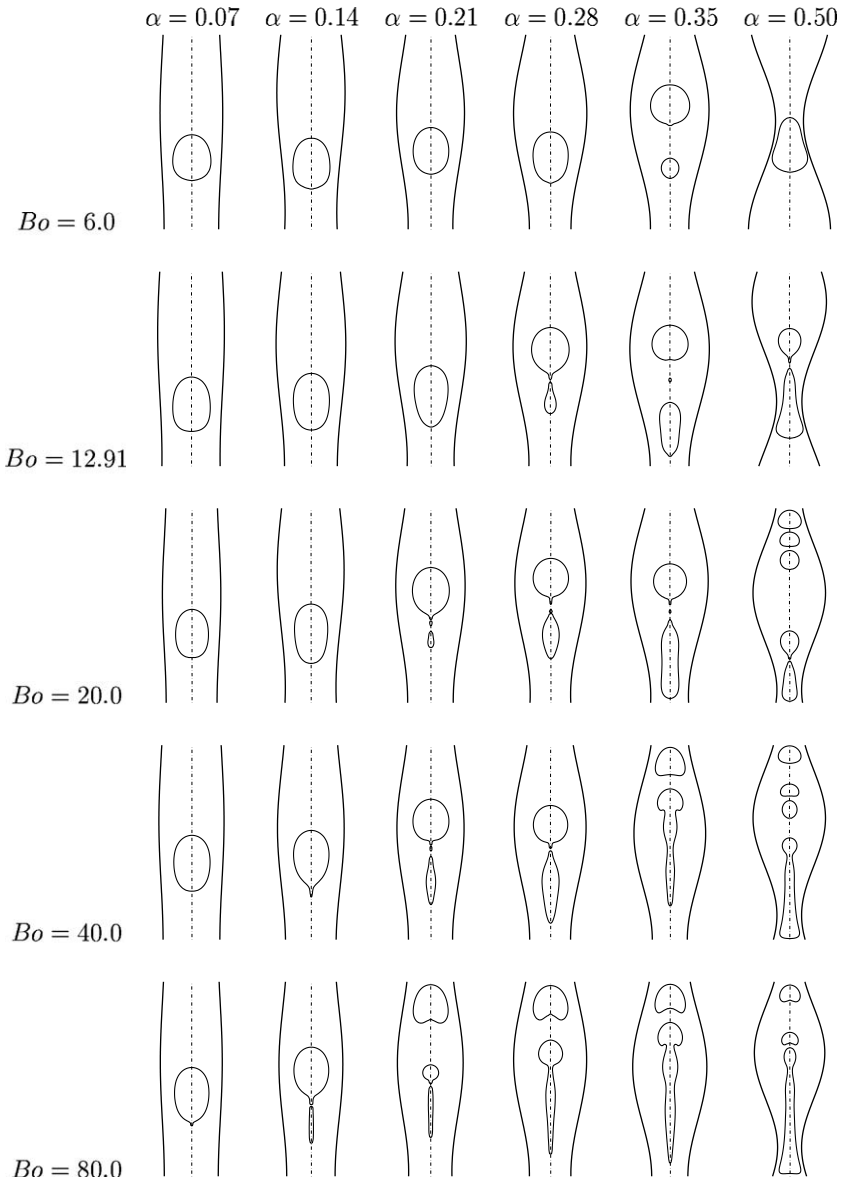

Fig. 12. Effects of the channel constriction and the Bond number on drop breakup. (Plots are not in the same scale and $\kappa = 0.70$.)

show the breakup mode at a high Bond number with a drop size equal or slightly larger than the critical value. As can be seen in this figure, this breakup mode resembles the tail streaming phenomena (Borhan and Pallinti, 1995, 1999). A drop breaks up into two or more drops with comparable sizes if the drop size is sufficiently larger than the critical drop size. A multiple drop breakup process is shown in Fig. 14 as a representative example for this breakup mode.

As discussed above, drop breakup occurs in various modes depending on the Bond number, the non-dimensional drop size and the channel geometry. We now investigate the conditions for the breakup. First the critical non-dimensional drop size is plotted in Fig. 15 as a function of the constriction parameter α for various Bond numbers ranging between 6 and 80. As can be seen in this figure, in general, the critical nondimensional drop size κ_{cr} decreases with increasing values of α; and for a fixed α, κ_{cr} decreases as the Bond number increases. For a fixed Bond number, a breakup can occur only for a range of constriction parameter α and

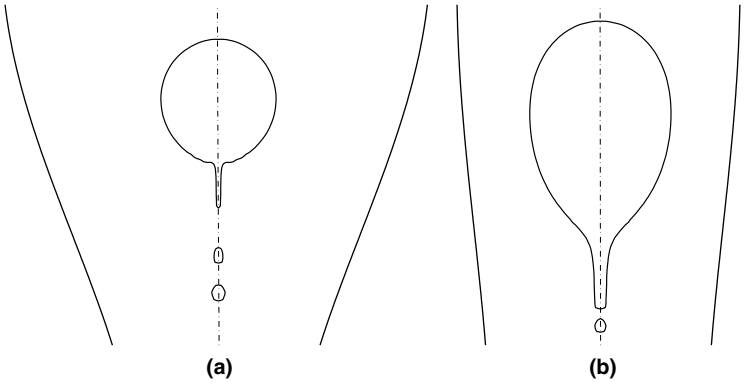

Fig. 13. Typical drop breakups at high Bond number and the critical drop size: (a) $Bo = 40.0$, $\alpha = 0.50$ and $\kappa = \kappa_{cr} = 0.41$; (b) $Bo = 80.0$, $\alpha = 0.14$ and $\kappa = \kappa_{cr} = 0.65$.

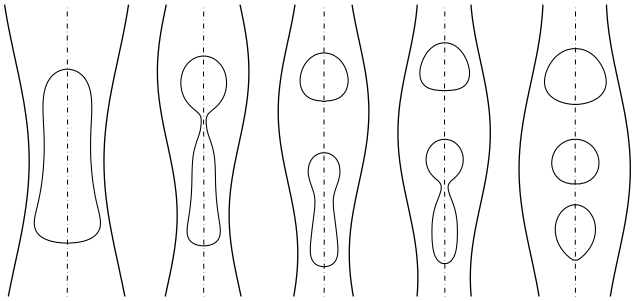

Fig. 14. Snapshots showing the evolution of a large drop in a constricted channel. Time progresses from left to right and plots are not in the same scale ($\kappa = 0.84$, $\kappa_{cr} = 0.68$, $\alpha = 0.28$ and $Bo = 12.91$).

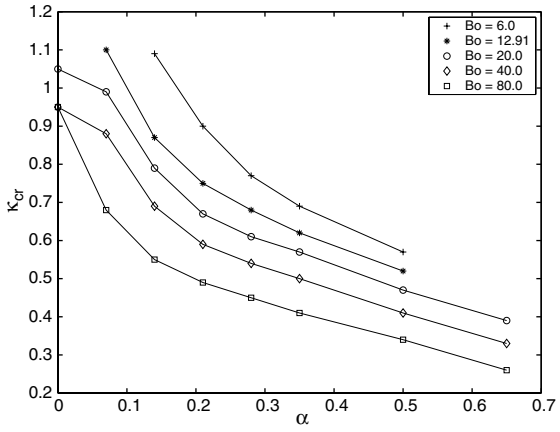

Fig. 15. Dimensionless critical drop size (κ_{cr}) as a function of the channel constriction parameter (α) for different values of Bond number.

the range gets narrower as the Bond number decreases. For instance, in the experimental conditions, i.e., $Bo = 12.91$, a breakup occurs in the range $0.08 < \alpha < 0.5$. In the case of a straight channel, it is found that a breakup occurs only if $Bo \gtrsim 20.0$. For smaller values of Bo, a breakup may not occur even in the constricted channels independent of drop size. On the other hand, if the constriction is too severe, i.e., α is large, and the buoyancy forces are not sufficient to force the drop through the constrictions, i.e., Bo is small, a drop gets stuck at the throat. In this case, hydrostatic conditions are eventually established as buoyancy forces are

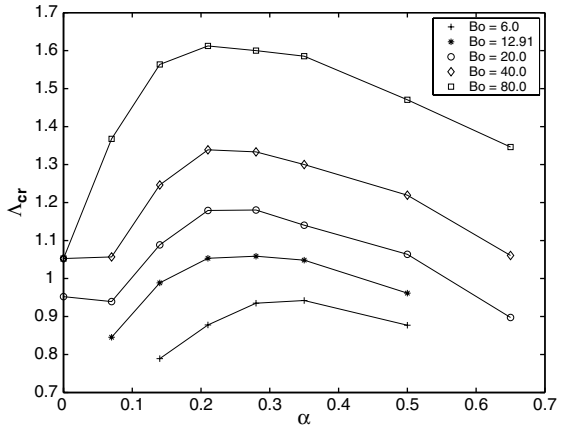

Fig. 16. The ratio of the channel radius at the throat to the critical drop radius ($\Lambda_{cr} = R/R_{d_{cr}}$) as a function of the channel constriction parameter (α) for different values of Bond number.

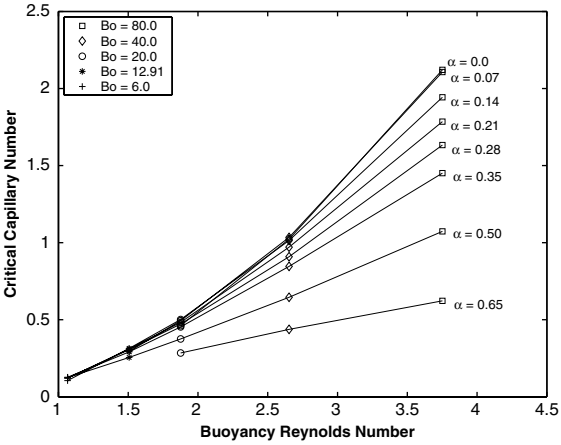

Fig. 17. Critical capillary number versus buoyancy Reynolds number for different values of channel constriction parameter α.

balanced by the surface tension forces as discussed before. Fig. 16 shows the ratio of the channel radius at the throat to the critical drop radius, $\Lambda_{cr} = R_{th}/R_{d_{cr}}$, as a function of the constriction parameter α for various values of the Bond number. As can be seen in this figure, Λ_{cr} generally increases with the Bond number. However it first increases, reaches a maximum and then decreases as α increases. This figure indicates that a breakup occurs most effectively at moderate values of α. Finally, critical capillary and buoyancy Reynolds numbers are defined as $Ca_{cr} = \mu U_{cr}/\sigma$ and $Re = (R^3 g \rho_o \Delta\rho)^{1/2}/\mu_o$, respectively, where U_{cr} is the average rise velocity of the drop at which a breakup occurs. The critical capillary number is plotted as a function of the buoyancy Reynolds number in Fig. 17 for various values of the Bond number and the constriction parameter α. It is clearly seen in this figure that the critical capillary number is essentially independent of the constrictions at small Bond numbers, i.e., $Bo < 6$ but it is increasingly influenced by the constrictions as the Bond number increases. It is also observed that the critical capillary number decreases as the constriction parameter increases.

4. Conclusions

Buoyancy-driven motion and breakup of viscous drops in constricted capillaries are studied computationally using a finite-volume/front-tracking method. Computational results are first compared with the available

experimental data and are found to be in a good agreement. The breakup modes of viscous drops are examined for a wide range of non-dimensional drop sizes, channel geometries and Bond numbers. It is found that a drop breakup occurs when the size of drop is larger than a critical value in various modes depending on the relative drop size, channel constriction and Bond number. When the Bond number is large, a drop breaks up into a large leading drop and many smaller trailing drops for the drop sizes equal or slightly larger than the critical value. This breakup mode resembles the tail streaming phenomena. As drop size is further increased, the size of the trailing drop increases such that the leading drop volume remains nearly constant and the trailing drop breaks up into still smaller drops until drop sizes are all smaller than the critical drop size. In other words, a large drop tends to produce mono-dispersed drops through series of breakups. The conditions for a drop breakup are also investigated. In general, the critical drop size decreases with increasing values of the constriction parameter α; and for a fixed α, the critical drop size decreases with the Bond number. If the constriction is too severe and Bond number is not sufficiently large to force the drop through the constriction, the drop gets stuck at a throat and hydrostatic conditions are established eventually. It is shown that a breakup occurs the most effectively in moderately constricted channels. The critical capillary number is found to be independent of the constriction parameter at small Bond numbers, i.e., $Bo < 6$ and it is increasingly influenced by the constrictions as the Bond number increases. It is also observed that the critical capillary number gets smaller as the channel constriction increases.

Acknowledgements

The computations are performed using the high performance computing center at Koc University. We thank the Scientific and Technical Research Council of Turkey (TUBITAK) (105M043) for partial support of this research.

References

Beam, R.M., Warming, R.F., 1978. An implicit factored scheme for the compressible Navier–Stokes equations. AIAA J. 16, 393–402.

Borhan, A., Pallinti, J., 1995. Buoyancy-driven motion of viscous drops through cylindrical capillaries at small Reynolds numbers. Ind. Eng. Chem. Res. 34, 2750–2761.

Borhan, A., Pallinti, J., 1999. Breakup of drops and bubbles translating through cylindrical capillaries. Phys. Fluids 11, 2846–2855.

Caughey, D.A., 1988. Diagonal implicit multigrid algorithm for the Euler equations. AIAA J. 26, 841–851.

Caughey, D.A., 2001. Implicit multigrid computation of unsteady flows past cylinders of square cross-section. Comput. Fluids 30, 939–960.

Fauci, L., Gueron, S. (Eds.), 2001. Computational Modeling in Biological Fluid Dynamics. Springer-Verlag, New York.

Gauglitz, P.A., Radke, C.J., 1990. The dynamics of liquid film breakup in constricted cylindrical capillaries. J. Colloid Interf. Sci. 134, 14–40.

Hemmat, M., 1996. The motion of drops and bubbles through sinusoidally constricted capillaries. Ph.D. Thesis, The Pennsylvania State University.

Hemmat, M., Borhan, A., 1996. Buoyancy-driven motion of drops and bubbles in a periodically constricted capillary. Chem. Eng. Commun. 150, 363–384.

Ho, B.P., Leal, L.G., 1975. The creeping motion of liquid drops through a circular tube of comparable diameter. J. Fluid Mech. 71, 361–383.

Larson, R.G., Davis, H.T., Scriven, L.E., 1981. Displacement of residual nonwetting fluid from porous media. Chem. Eng. Sci. 36, 75–85.

Muradoglu, M., Gokaltun, S., 2004. Implicit multigrid computations of buoyant light drops through sinusoidal constrictions. J. Appl. Mech.—Trans. ASME 71, 857–865.

Muradoglu, M., Kayaalp, A.D., 2006. An auxiliary grid method for computations of multiphase flows in complex geometries. J. Comput. Phys. 214, 858–877.

Olbricht, W.L., 1996. Pore-scale prototypes of multiphase flow in porous media. Ann. Rev. Fluid Mech. 28, 187–213.

Olbricht, W.L., Leal, L.G., 1983. The creeping motion of immiscible drops through a converging/diverging tube. J. Fluid Mech. 134, 329–355.

Pozrikidis, C. (Ed.), 2003. Modeling and Simulation of Capsules and Biological Cells. Chapman & Hall/CRC Press, Boca Raton.

Stone, H.A., 1994. Dynamics of drop deformation and breakup in viscous fluids. Ann. Rev. Fluid Mech. 26, 65–102.

Stone, H.A., Stroock, A.D., Ajdari, A., 2004. Engineering flows in small devices: microfluidics toward lab-on-a-chip. Ann. Rev. Fluid Mech. 36, 381–411.

Tryggvason, G., Bunner, B., Esmaeeli, A., Juric, D., Al-Rawahi, N., Tauber, W., Han, J., Nas, S., Jan, Y.-J., 2001. A front-tracking method for the computations of multiphase flow. J. Comput. Phys. 169, 708–759.

Tsai, T.M., Miksis, M.J., 1994. Dynamics of a drop in a constricted capillary tube. J. Fluid Mech. 274, 197–217.
Tsai, T.M., Miksis, M.J., 1997. The effects of surfactant on the dynamics of bubble snap-off. J. Fluid Mech. 337, 381–410.
Unverdi, S.O., Tryggvason, G., 1992. A front-tracking method for viscous incompressible multifluid flows. J. Comput. Phys. 100, 25–37.
Westborg, H., Hassager, O., 1989. Creeping motion of long bubbles and drops in capillary tubes. J. Colloid Interf. Sci. 133, 135–147.